

---

# Towards Reliable Detection of Empty Space: Conditional Marked Point Processes for Object Detection

---

**Tobias J. Riedlinger\***

Technical University of Berlin  
Berlin, Germany  
riedlinger@math.tu-berlin.de

**Kira Maag\***

Heinrich-Heine-University Düsseldorf  
Düsseldorf, Germany  
kira.maag@hhu.de

**Hanno Gottschalk**

Technical University of Berlin  
Berlin, Germany  
gottschalk@math.tu-berlin.de

## Abstract

Deep neural networks have set the state-of-the-art in computer vision tasks such as bounding box detection and semantic segmentation. Object detectors and segmentation models assign confidence scores to predictions, reflecting the model's uncertainty in object detection or pixel-wise classification. However, these confidence estimates are often miscalibrated, as their architectures and loss functions are tailored to task performance rather than probabilistic foundation. Even with well calibrated predictions, object detectors fail to quantify uncertainty outside detected bounding boxes, i.e., the model does not make a probability assessment of whether an area without detected objects is truly free of obstacles. This poses a safety risk in applications such as automated driving, where uncertainty in empty areas remains unexplored. In this work, we propose an object detection model grounded in spatial statistics. Bounding box data matches realizations of a marked point process, commonly used to describe the probabilistic occurrence of spatial point events identified as bounding box centers, where marks are used to describe the spatial extension of bounding boxes and classes. Our statistical framework enables a likelihood-based training and provides well-defined confidence estimates for whether a region is drivable, i.e., free of objects. We demonstrate the effectiveness of our method through calibration assessments and evaluation of performance.

## 1 Introduction

Deep neural networks (DNNs) have demonstrated outstanding performance in computer vision tasks like image classification Wortsman et al. [2022], object detection Zong et al. [2023], instance segmentation Yan et al. [2023] and semantic segmentation Xu et al. [2023]. Object detection describes the task of identifying and localizing objects of a particular class, for example, by predicting bounding boxes or by labeling each pixel that corresponds to a certain instance. Semantic segmentation corresponds to assigning each pixel in an image to one of a predefined set of semantic classes. These tasks serve as an indispensable tool for scene understanding, providing precise information about the scenario. The application areas for computer vision tasks are diverse, including in safety-critical areas, for example in robotics Cartucho et al. [2021], medical diagnosis Kang and Gwak

---

\*Equal contribution.



Figure 1: *Left*: Semantic segmentation prediction. *Center left*: Poisson point process intensity. *Center right*: Conditional marked Poisson point process intensity. *Right*: Bounding box prediction.

[2019] and automated driving Xu et al. [2023]. Along with a strong performance of the models, prediction reliability in the form of uncertainty assessment Maag and Riedlinger [2024] and calibrated confidence estimates Mehrtaah et al. [2019] is also highly relevant.

Object detectors provide confidence values (“objectness score”) about the correctness of each predicted object, while semantic segmentation models output a score per pixel indicating the confidence of class affiliation. Both of the former represent the probability of correctness, which also reflects the uncertainty of the model with respect to its prediction. For well-calibrated scores, we expect that the assigned confidence matches the observed prediction accuracy, i.e., out of 100 predictions with a confidence of 70% each, 70 are correct. However, confidence given by DNNs are frequently miscalibrated, with confidence values not matching the observed accuracy Küppers et al. [2022]. This problem is oftentimes tackled by confidence calibration methods which regularize the training objective or rectify calibration in post-processing Guo et al. [2017]. Methods like Monte-Carlo (MC) Dropout Gal and Ghahramani [2016] and deep ensembles Lakshminarayanan et al. [2017], are often used as approximations to model uncertainty and do not necessarily lead to better calibration.

The problem of miscalibration often arises from a mis-specification of the architecture and/or the loss function of the model. The logic of stochastically independent pixel-wise predictions like in semantic segmentation or objectness are violated in practice. Architectures are often created based on heuristics and practical considerations, e.g., feature pyramid networks Lin et al. [2017] or anchor box procedures Redmon et al. [2016], working well empirically but lacking a probabilistic foundation. Moreover, the commonly used cross-entropy loss is also not intrinsically designed for probability calibration, since its main goal is to optimize classification accuracy Liu et al. [2024]. In doing so, the DNN is likely to predict the true class with high probability, without correctly calibrating the probabilities of the other classes. Models tend to predict extremely high or low probabilities, resulting in overconfidence.

Even if the uncertainties/confidences of the predictions are correctly calibrated, there is a particular problem in object detection, namely that areas outside identified objects are ignored. The object detector does not provide an explicit uncertainty quantification for the areas outside their predictions, i.e., the model does not make a probability assessment of whether an area without detected objects is truly free of obstacles. Such models are often overconfident in assuming that “no object” means the area is safe. In applications such as automated driving, this is a shortcoming, as there is no probability information about the safety of empty areas.

In this work, we propose an object detection model based on spatial statistics, regarding bounding box data as realizations of a marked point process Møller et al. [2003], Sherman [2011]. Such models have been used to model spatial phenomena, e.g., in astronomy, spatial epidemiology or geostatistics, to describe the probabilistic occurrence of spatial point events. Further, adding a mark to each point event describing the spatial extension of the object (width and height) and classes, we obtain an object detection model based on the logic of counting processes. When conditioned on the number of events, our model design enables likelihood-based training. As such, our model exhibits well-defined notions of confidence for the event that a certain region in space is drivable (devoid of objects). Regarding the unmarked point process, i.e., predicting only the object center points, counting zero objects in some region is then seen as the region being drivable. Including the marks (object detection), we may ask for the model’s probability that a certain region does not intersect any of the marked points giving rise to an object detector which defines confidences that any region in space is truly free. An exemplary prediction is shown in Figure 1.

We summarize our contribution as follows:

- We develop a deep learning framework for modeling the intensity function of spatial point processes based on a negative log-likelihood loss function.
- We propose a principled model for object detection based on the theory of marked Poisson point processes and evaluate the model on street scene data.
- We propose an evaluation protocol for testing calibration of empty space detection. The proposed model is shown to be well-calibrated on image regions while having comparable performance to standard object detection architectures.

To our knowledge, this is the first time, a spatial statistics approach has been used for deep object recognition in computer vision. Our derivation of the loss function is a principled and mathematically underpinned approach to deep object detection showing both, parallels but also differences with typical design choices in object detection. The source code of our method is publicly available at <https://github.com/tobiasriedlinger/cmppp-object-detection>.

## 2 Related work

**Confidence calibration.** To measure the miscalibration, the expected calibration error (ECE) error is frequently used Guo et al. [2017] where all samples of a dataset are binned based on their predicted confidence information to measure the accuracy in each bin, which is an approximation to the definition of calibration. On the one hand, binning techniques were developed, for example histogram binning Zadrozny and Elkan [2001], isotonic regression Zadrozny and Elkan [2002] and Bayesian binning Naeini et al. [2015], which group all samples by their predicted confidence and assign the observed bin accuracy as a calibrated confidence to the grouped samples. On the other hand, scaling methods were considered, e.g. Platt scaling Platt [1999], temperature scaling Guo et al. [2017], beta calibration Kull et al. [2017] and Dirichlet calibration Kull et al. [2019], which rescale the logits before sigmoid or softmax operation to obtain calibrated confidence estimates, but differ in their assumptions about the input data and the resulting recalibration scheme. Scaling methods achieve good calibration performance given only a small amount of samples compared to binning methods, but are limited by the underlying parametric assumptions. For this reason, combinations of both approaches have been developed Ji et al. [2019], Kumar et al. [2019]. Another strategy for confidence calibration is to adjust the optimization objective during model training Pereyra et al. [2017], Kumar et al. [2018], Mukhoti et al. [2020], Fernando and Tsokos [2022].

The aim of confidence calibration is to assess uncertainties correctly in order to make reliable decisions. Particularly in the case of object detection, the focus is on correctly calibrating the existence of objects, while overlooked objects are ignored. This is the contrary perspective to our work, as we reliably predict empty (*and* occupied) spaces enabling a safe drive.

**Drivable area prediction.** Drivable area or free space detection does not focus on objects, but on the classification between drivable and background (everything else). This can be done based on various sensors such as LiDAR, radar, camera and aerial imaging Hortelano et al. [2023] where our focus is on camera data. The basis for the drivable area prediction is often a semantic segmentation architecture, since pixel level predictions are considered Chen et al. [2025], Qiao and Zulkernine [2021]. Different network design choices have been pursued to solve drivable area prediction including fully convolutional models Yu et al. [2023], Chan et al. [2019], incorporation of LSTM layers Lyu et al. [2019] or boundary attention units Sun et al. [2019] to overcome task-specific difficulties. Another approach to improve the drivable area detection involves multi-task architectures, e.g., for different segmentation tasks Lee [2021], detection of lane lines Wang et al. [2024] or instance segmentation Luo et al. [2024]. In Qian et al. [2020], a unified neural network is constructed to detect drivable areas, lane lines and traffic objects using sub-task decoders to share designate influence among tasks. In addition to combining tasks, different types of sensor data can also help, such as combining RGB images with depth information Fan et al. [2020], Jain et al. [2023]. An uncertainty-aware symmetric network is presented in Chang et al. [2022] to achieve a good trade-off between speed and accuracy by fully fusing RGB and depth data.

In contrast to our methodology, drivable area prediction and free space detection are based on design choices and practical considerations and do exhibit well-defined notions of confidence.

### 3 Method description

#### 3.1 Marked point process models

A statistical model has to reflect the structure of the data. In object detection, the data describing an instance consists of data  $z = (\xi, m)$ , where  $\xi = (\xi_x, \xi_y) \in [0, 1]^2$  encodes the location of the instances' center on a given image, while  $m = (h, w, \kappa) \in \mathbb{R}^2 \times \mathcal{C}$  gives additional information, namely height and width of the bounding box and a label  $\kappa$  from a discrete set of classes  $\mathcal{C}$ . We address  $\xi$  as point location and  $m$  as "marks" that further specify the information on the point  $\xi$ .

The data for object detection for a given image consists of a set  $\{z_1, \dots, z_n\}$  of marked points, where  $n \in \mathbb{N}_0$  is not fixed across different images. If we assume that  $\xi_j \neq \xi_k$  for  $j \neq k$ , we see that the locations  $\{\xi_1, \dots, \xi_n\} \subseteq [0, 1]^{2 \times s^n}$  form a finite set of discrete points. Here the symmetrized product space  $[0, 1]^{2 \times s^n}$  is obtained by mapping  $(\xi_1, \dots, \xi_n) \in [0, 1]^{2n}$  to  $\{\xi_1, \dots, \xi_n\}$ . Let  $\Gamma = \bigoplus_{n \in \mathbb{N}_0} [0, 1]^{2n} \setminus D_n$  be the configuration space of finite point patterns on  $[0, 1]^2$ , where the diagonal  $D_n = \{\{\xi_1, \dots, \xi_n\} : \xi_l \in [0, 1]^2, l \in [1 : n] \exists (j, k) \in [1 : n], j \neq k, \xi_j = \xi_k\}$  is taken out to avoid ambiguity between points. We identify  $[0, 1]^{2 \times 0} \setminus D_0 = \{e\}$  with the "empty configuration"  $e = ()$ , which contains  $n = 0$  points. Let  $(\Omega, \mathcal{A}, \mathbb{P})$  be a probability space, then any random variable  $X : \Omega \rightarrow \Gamma$  is called a (spatial) point process over  $[0, 1]^2$ , and  $N(A) = |X \cap A|$  the associated counting process counting the number of points  $X(\omega) = (\xi_1(\omega), \dots, \xi_{N(\omega)}(\omega))$  inside the measurable set  $A \subseteq [0, 1]^2$ . Note that clearly  $N(\omega) = N([0, 1]^2)(\omega)$  gives the total count of points for the given random parameter  $\omega \in \Omega$ .

Likewise, a marked point process  $X_M : \Omega \rightarrow \Gamma_M$  has configuration space  $\Gamma_M = \Gamma \times M^n$ , where the mark space  $M$  in our case is given by  $M = \mathbb{R}^2 \times \mathcal{C}$ . Given a marked point process, we can derive the corresponding simple point process by the projection  $X = \Pi X_M$ , where  $\Pi : \Gamma_M \rightarrow \Gamma$  is defined by  $\{z_1, \dots, z_n\} \mapsto \{\xi_1, \dots, \xi_n\}$ . It is clear that any marked point process can also be considered as a simple point process over the extended space  $[0, 1]^2 \times M$  and thus is associated with the counting process  $N_M(A_M) = |X_M \cap A_M|$ , where  $A_M \subseteq [0, 1]^2 \times M$ . Alternatively,  $N = \sum_{\xi \in X} \delta_\xi$  where  $\delta_\xi$  is the Dirac measure with mass one in  $\xi$  gives another representation of the counting process from which one easily sees that  $X$  and  $N$  encode the same information.

We are interested in statistical models that are eligible to model the distribution of a (marked) point process  $X_{(M)}$ . Here we suggest to use the Poisson point process (PPP) as the simplest model and "workhorse" of spatial statistics. It is based on an intensity measure  $\Lambda = \Lambda(z) dz$ , where  $dz$  is the Lebesgue measure on  $[0, 1]^2 \times \mathbb{R}^2 \times \mathcal{C}$  where on  $\mathcal{C}$  we chose the measure that counts the elements of a given subset. For  $A_M \subseteq [0, 1]^2 \times M$  specify the statistics of  $N_M(A_M)$  using the Poisson distribution with intensity  $\int_{A_M} \Lambda(z) dz$ , i.e., the probability of finding  $n \in \mathbb{N}_0$  instances with spatial-mark configurations in the set  $A_M$  is given by

$$\mathbb{P}(N_M(A_M) = n) = \frac{1}{n!} \left( \int_{A_M} \Lambda(z) dz \right)^n \exp \left( - \int_{A_M} \Lambda(z) dz \right) . \quad (1)$$

Choosing  $A_M = A \times M$  where  $A \subseteq [0, 1]^2$  is measurable, also the projected "center point process" of detection boxes,  $N(A)$ , is a Poisson point process with intensity on  $[0, 1]^2$  given by

$$\lambda(\xi) = \int_M \Lambda(\xi, m) dm . \quad (2)$$

#### 3.2 Conditional marked PPP as object detector

While eq. (1) provides a probabilistic model for the bounding box data  $\{z_1, \dots, z_n\}$  on a fixed image  $I$ , the distribution of the marked points may generally vary with respect to the input image  $I$ . Hence we have to model  $\Lambda(z) = \Lambda(z|I)$  as an intensity conditioned on the input  $I : [0, 1]^2 \mapsto [0, 1]^3$ , where the output dimensions represent the RGB-channels of the image. Through discretization,  $I$  is pixelized  $I_d : P \rightarrow [0, 1]^3$ , e.g. by integration over pixels. We set  $P = (\varepsilon_x(\mathbb{N} - \frac{1}{2}) \times \varepsilon_y(\mathbb{N} - \frac{1}{2})) \cap [0, 1]^2$  as the set of pixel center points with  $\frac{1}{\varepsilon_{x/y}} \in \mathbb{N}$  the number of pixels in  $x$  and  $y$  direction, respectively (in our case,  $\varepsilon_x = 1 = \varepsilon_y$ ). We call models in this class CMPPP models.

Let us now consider suitable models for OD from CMPPP. We take a factorizing approach to  $\Lambda$  in (2)

$$\Lambda(z|I) = \Lambda(\xi, m|I) = \tilde{\lambda}(\xi|I) \cdot p(m|\xi, I), \quad (3)$$

where  $\Lambda(z) \geq 0$  and  $p(m|\xi)$  is a Markov kernel that models the probability density of finding the mark  $m = (h, w, \kappa)$  given that there is a bounding box centered in  $\xi$ . Since  $\int_M p(m|\xi, I) dm = 1$  for all  $\xi \in [0, 1]^2$ ,  $\tilde{\lambda}(\xi) = \lambda(\xi)$  follows from eq. (2) and eq. (3). It remains to model the conditional intensity and the conditional probability on mark space as follows

$$\begin{aligned} \lambda_{\theta_L}(\xi|I_d) &= \exp(L_{\theta_L}(\xi, I_d)) \\ p_{\theta_B, \theta_C, \sigma^2}(m|\xi, I_d) &= \frac{1}{2\sigma} e^{-\frac{1}{\sigma} \| \binom{w}{h} - B_{\theta_B}(\xi, I_d) \|_1} \times [\text{softmax}(C_{\theta_C}(\xi, w, h, I_d))]_{\kappa} . \end{aligned} \quad (4)$$

Here  $L_{\theta_L}$  is a fully convolutional neural network (FCNN).  $B_{\theta_B}$  is a network with values in  $\mathbb{R}^2$  that processes the (discretized) image with convolutional layers and a head containing fully connected output layers. As usual in object detection, the regression is carried out to minimize the mean absolute deviation and not the squared residuals. This corresponds to utilizing a Laplace distribution in eq. (4) instead of a normal distribution. It provides an estimate of height and width of a bounding box under the hypothesis that an instance is centered at  $\xi$ . Finally,  $C_{\theta_C}$  is an image classification network with values in  $\mathbb{R}^q$ . It can be applied, e.g., to the clip of the discrete image  $I_d$  specified by the center point  $\xi$  and the estimated box height and width  $B_{\theta_B}(\xi, I_d)$ . Alternatively, one can provide the additional input of the classification location  $\xi$ , and not utilize the output of  $B_{\theta_B}$  in the class prediction.

### 3.3 Training the CMPPP model

Likelihood-based training is applied in most machine learning approaches. Here one utilizes the negative log-density function with respect to the Lebesgue measure as loss function, i.e.,  $\ell(x, \theta) = -\log f_{\theta}(x)$  where  $X \sim \mu_{\theta} = f_{\theta}(x) dx$  is a hypothesis on the distribution of the data represented by (independent copies of) the random variable  $X : \Omega \rightarrow \mathbb{R}^d$ . This is no longer feasible in the setting of point processes  $X : \Omega \rightarrow \Gamma$  as no Lebesgue measure  $dx$  exists on the infinite dimensional space  $\Gamma$  and therefore the notion of a density w.r.t.  $dx$  is ill-defined.

The notion of a likelihood can however be adapted to reference measures that are different from the Lebesgue measure. Let, in the finite dimensional setting,  $\mu$  be another probability measure on  $\mathbb{R}^d$  with density  $f_{\mu}(x)$  such that  $f_{\mu}(x) = 0$  implies  $f_{\theta}(x) = 0$ . We obtain

$$\ell(x, \theta) = -\log f_{\theta}(x) = -\log \frac{f_{\theta}(x)}{f_{\mu}(x)} - \log f_{\mu}(x) = -\log \left( \frac{d\mu_{\theta}}{d\mu}(x) \right) - \log f_{\mu}(x) . \quad (5)$$

Here  $\frac{d\mu_{\theta}}{d\mu}(x) = \frac{f_{\theta}(x)}{f_{\mu}(x)}$  is the Radon-Nikodym derivative of  $\mu_{\theta}$  with respect to the reference measure  $\mu$ . As the gradients  $\nabla_{\theta} \ell(x, \theta)$  of eq. (5) do not depend on the second term on the right hand side, training with the negative log likelihood loss is equivalent to training with the negative log-Radon Nikodym derivative. Furthermore, the gradients also do not depend on the particular choice of  $\mu$ , provided the Radon-Nikodym derivative exists.

The training of stochastic models with an infinite dimensional state space is based on the insight that Radon-Nikodym derivatives with respect to adequately chosen reference measures  $\mu$  still exist, as long as  $\mu_{\theta} = \tilde{f}_{\theta} \mu$  holds, where the relative density  $\tilde{f}_{\theta}(x) = \frac{d\mu_{\theta}}{d\mu}(x)$  again is the Radon-Nikodym derivative at  $x \in \Gamma$ . As the reference measure, we choose the distribution  $\mu$  of the PPP with intensity function identically equal to one. The Radon-Nikodym derivative of the distribution of a PPP  $\mu_{\theta}$  with intensity  $\lambda_{\theta}(\xi)$  w.r.t.  $\mu$  then is

$$\frac{d\mu_{\theta}}{d\mu}(x) = \left( \prod_{l=1}^n \lambda_{\theta}(\xi_l) \right) e^{-\int_{[0,1]^2} (\lambda_{\theta}(\xi) - 1) d\xi}, \quad x = \{\xi_1, \dots, \xi_n\} \in \Gamma . \quad (6)$$

This identity is a standard exercise in textbooks on spatial statistics, see, e.g., Daley and Vere-Jones [2006]. For the convenience of the reader we provide a proof in appendix A.1. Equation (6) immediately generalizes to marked CMPPP if we replace  $x \in \Gamma$  with  $x = \{z_1, \dots, z_n\} \in \Gamma_M$ ,  $\lambda_{\theta}(\xi_l)$  with  $\lambda_{\theta}(z_l|I)$ ,  $\xi$  with  $z$ ,  $[0, 1]^2$  with  $[0, 1]^2 \times M$  and  $d\xi$  with  $dz$ .

Inserting eq. (3) and eq. (4) into the updated version of eq. (6) and taking the negative logarithm, we obtain the loss function

$$\begin{aligned} \ell(x, \theta) = & \int_{[0,1]^2} e^{L_{\theta_L}(\xi, I_d)} d\xi - \sum_{l=1}^n L_{\theta_L}(\xi_l, I_d) \\ & + \sum_{l=1}^n \frac{1}{\sigma} \left\| \begin{pmatrix} w_l \\ h_l \end{pmatrix} - B_{\theta_B}(\xi_l, I_d) \right\|_1 + n \log(2\sigma) \\ & - \sum_{l=1}^n \left[ C_{\theta_C, \kappa}(\xi_l, w_l, h_l, I_d) + \log \left( \sum_{\kappa' \in \mathcal{C}} e^{C_{\theta_C, \kappa'}(\xi_l, w_l, h_l, I_d)} \right) \right], \end{aligned} \quad (7)$$

where  $\theta = (\theta_L, \theta_B, \theta_C, \sigma^2)$  are the model parameters and  $z = \{z_1, \dots, z_n\} \in \Gamma_M$  the bounding box configurations observed in the image  $I$ . A step by step derivation of eq. (7) can be found in appendix A.1. Minimizing the loss function now enables a strictly likelihood based training.

It is now easy to interpret the top line of eq. (7) as the loss for the intensity function and hence a loss for a distributed objectness score, the middle line as  $L^1$ -loss of bounding box regression and the bottom line as standard negative log likelihood (“cross entropy”) loss of an image classifier. The integral in the top line is discretized as

$$\int_{[0,1]^2} e^{L_{\theta_L}(\xi, I_d)} d\xi \approx \sum_{\pi \in P} e^{L_{\theta_L}(\pi, I_d)} \varepsilon_x \varepsilon_y. \quad (8)$$

We note that the training of width and height prediction  $B_{\theta_B}$  is independent of the value of the scale variable  $\sigma > 0$  acting as dispersion parameter and can be conducted first and result in the optimal weights  $\hat{\theta}_B$ . Thereafter, the maximum likelihood equations for  $\sigma$  give  $\sigma = \frac{1}{n} \sum_{l=1}^n \left\| \begin{pmatrix} w_l \\ h_l \end{pmatrix} - B_{\hat{\theta}_B}(\xi_l, I_d) \right\|_1$ , hence  $\sigma$  is estimated as the mean average deviation of the bounding box regression.

### 3.4 Probabilistic predictions of empty space

On the basis of a trained model with parameters  $\hat{\theta}$  we now derive a probabilistic conditional prediction that a region  $A \subseteq [0, 1]^2$  is “free of objects”. This statement can be interpreted in different ways. On the one hand, we can interpret it as “free of object centers”. As the random variable  $X$  is our model for object centers and  $N = \delta_X$  is the associated counting measure, the event that  $A$  is free amounts to  $X \cap A = \emptyset$  or  $N(A) = 0$ . Using eq. (1) for  $\lambda_{\hat{\theta}_L}(\cdot | I_d) = \exp(L_{\hat{\theta}_L}(\cdot | I_d))$  instead of  $\Lambda$ , we obtain

$$\mathbb{P}_{\hat{\theta}}(N(A) = 0 | I_d) = \exp \left( - \int_A \lambda_{\hat{\theta}_L}(\xi | I_d) d\xi \right), \quad (9)$$

where the integral in the exponent is evaluated as in eq. (8) with  $P$  replaced by  $A \cap P$ .

On the other hand, we can interpret the statement “ $A$  is free of objects” as the event that  $A$  does not intersect any of the bounding boxes  $[\xi_x - \frac{w}{2}, \xi_x + \frac{w}{2}] \times [\xi_y - \frac{h}{2}, \xi_y + \frac{h}{2}] =: b(z)$  for any  $z = (\xi_x, \xi_y, w, h, \kappa) \in X_M$  arbitrary.

Let us consider the critical set for  $\xi \in A$ , i.e., the set of all bounding box configurations  $D^c(\xi) \subseteq [0, 1]^2 \times M$  such that a given point  $\xi$  is contained in the corresponding bounding box. It is easily seen that  $D^c(\xi) = \{z' = (\xi', w', h', \kappa') \in [0, 1]^2 \times M : |\xi_x - \xi'_x| \leq w/2 \text{ and } |\xi_y - \xi'_y| \leq h/2\}$ . The critical set for the entire region  $A$  then obviously is given by  $D^c(A) = \bigcup_{\xi \in A} D^c(\xi)$  and the probability that no bounding box in a given image  $I$  intersects  $A$  is

$$\mathbb{P}_{\hat{\theta}}(N(D^c(A)) = 0 | I) = \exp \left( - \int_{D^c(A)} \Lambda_{\hat{\theta}_L}(z | I) dz \right), \quad (10)$$

where  $\Lambda(z | I)$  is evaluated using eq. (3) and eq. (4). Let us shortly consider the evaluation of the integral on the right hand side of eq. (10). By our conditional modeling ansatz, the integral over  $\Lambda_{\hat{\theta}}$  separates to

$$\int_{[0,1]^2 \setminus A} \lambda_{\hat{\theta}_L}(\xi | I) \int_{\{m \in M : b(\xi, m) \cap A \neq \emptyset\}} p(m | \xi, I) dm d\xi. \quad (11)$$

If the test region  $A$  is a rectangle with center point  $\xi^A \in [0, 1]^2$ , width  $w^A$  and height  $h^A$ , we have that  $A$  intersects  $b(\xi, w, h, \kappa)$  if both,  $|\xi_x^A - \xi_x| \leq \frac{1}{2}(w^A + w)$  and  $|\xi_y^A - \xi_y| \leq \frac{1}{2}(h^A + h)$  hold.

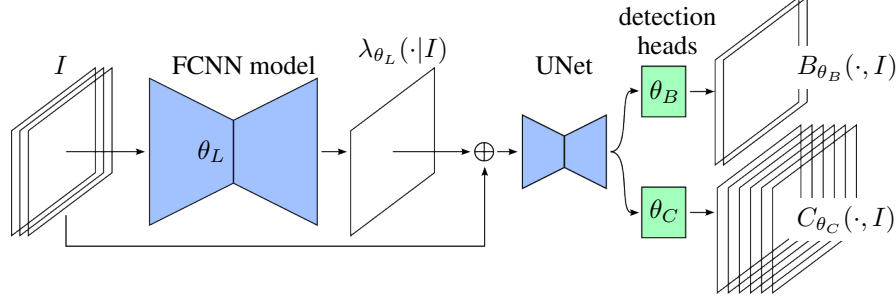


Figure 2: Proposed object detection architecture based on a first-stage FCNN model for the intensity function. The second stage consists of a UNet encoder-decoder model with two heads, one predicting the spatial extension of bounding boxes and the other one classification. The second stage model is trained separately from first stage on original input images and intensity predictions.

The inner integral, therefore, factorizes and the integral in eq. (10) becomes

$$\int_{[0,1]^2 \setminus A} \lambda_{\hat{\theta}_L}(\xi|I) \int_{2|\xi_x^A - \xi_x| - w^A}^{\infty} \frac{1}{2\sigma} e^{-\frac{1}{\sigma}|w - B_{\hat{\theta}_B}^w(\xi, I)|} dw \int_{2|\xi_y^A - \xi_y| - h^A}^{\infty} \frac{1}{2\sigma} e^{-\frac{1}{\sigma}|h - B_{\hat{\theta}_B}^h(\xi, I)|} dh d\xi \quad (12)$$

which can easily be expressed by the cumulative distribution function (e.g.,  $1 - F(B_{\hat{\theta}_B}^w(\xi, I))$ ) of the distribution used to model  $w$  and  $h$ . This way, the evaluation of the void confidence generalizes e.g., to modeling with normal distributions and can easily be algorithmically implemented. While the inner integral over  $\{m \in M : b(\xi, m) \cap A \neq \emptyset\}$  may in general be computed by logical querying of pixels and CDFs, more general shapes may also be treated via the inclusion-exclusion principle.

## 4 Experiments

### 4.1 Model design

**Network architecture.** The training protocol is guided by the interdependency of the parameters  $\theta_L, \theta_B$  and  $\theta_C$  of the three neural networks  $L, B$  and  $C$ . If parameters, e.g., in the model’s backbone, are shared, all parameters in  $\theta$  can be trained jointly in a one shot manner. However, one can also choose to disentangle the training of  $\theta_L, \theta_B, \theta_C$  in stages, if not all parameters are shared. In this work we, follow the latter protocol depicted in Figure 2. The hierarchical model we introduce builds on a semantic segmentation model with one output channel modeling the intensity function  $\lambda$  by  $\theta_L$ . As in the first stage, the regression and classification heads are frozen, the loss function for  $\theta_L$  involves only the first line in eq. (7) with object center points as point configuration. We utilize an exponential activation for the intensity function. For the second stage training, we now freeze  $\hat{\theta}_L$ . The RGB input image  $I$  is concatenated with  $\lambda_{\hat{\theta}_L}$  and fed through a UNet architecture for secondary feature extraction after which the features are interpolated back to input shape and concatenated. Two-layer detection heads predict width and height ( $\theta_B$ ) and the class affiliation ( $\theta_C$ ), respectively. The feature maps  $B$  and  $C$  are evaluated at the point configuration and trained with the second and third line of eq. (7) with available ground truth information. While  $B$  and  $C$  are computed from the shared parameters in the UNet model, they are disentangled and conditioned on the intensity  $\lambda_{\hat{\theta}_L}$ .

**Prediction.** For bounding box prediction, instead of the standard non-maximum suppression algorithm, we exploit the counting statistics of the spatial point process and determine the number of expected points from  $\mathbb{E}[N] = \int_{[0,1]^2} \lambda_{\hat{\theta}_L}(\xi|I) d\xi$ . Afterwards, we extract as many peaks from the intensity heatmap as determined in this manner to find the predicted center points. As the intensity function is sharply peaked but still somewhat smooth, we crop square regions of  $20 \times 20$  pixels around determined maxima before searching for the next peak. Marks are determined simply by evaluation of  $B_{\hat{\theta}_B}$  and  $C_{\hat{\theta}_C}$  heatmaps at the respectively determined center points.

Table 1: Calibration values for semantic segmentation ( $ECE_S$ ) and our PPP method ( $ECE_P$ ) for different box sizes  $s$ .

|             | $s$     | 250    | 500    | 750    | 1,000  | 1,500  | 2,500  | 5,000  | 10,000 |
|-------------|---------|--------|--------|--------|--------|--------|--------|--------|--------|
| Deep-Labv3+ | $ECE_S$ | 0.1102 | 0.1741 | 0.2033 | 0.2309 | 0.2521 | 0.2667 | 0.2417 | 0.1948 |
|             | $ECE_P$ | 0.0012 | 0.0021 | 0.0029 | 0.0030 | 0.0051 | 0.0086 | 0.0120 | 0.0184 |
| HRNet       | $ECE_S$ | 0.0413 | 0.0859 | 0.1142 | 0.1443 | 0.1785 | 0.2206 | 0.2295 | 0.1939 |
|             | $ECE_P$ | 0.0014 | 0.0019 | 0.0027 | 0.0032 | 0.0049 | 0.0085 | 0.0121 | 0.0177 |

## 4.2 Experimental setting

**Models.** The architecture of our PPP model is implemented in the MMDetection environment Chen et al. [2019] and based on fully convolutional neural networks commonly used for the semantic segmentation task, i.e., DeepLabv3+ Chen et al. [2018] with ResNet-50 backbone and HRNet Wang et al. [2021]. Our used UNet Ronneberger et al. [2015] architecture has 5 stages with a base channel number of 16. The detection and classification heads are two-layer convolutional models separated by one ReLU activation. Training ran on a Nvidia A100 GPU with 80GBs of memory.

**Datasets.** In our experiments, we use the Cityscapes dataset Cordts et al. [2016], which depicts dense urban traffic scenarios in various German cities. This dataset consists of 2,975 training images and 500 validation images of size  $1,024 \times 2,048$  from 18 and 3 different cities, respectively, with labels for semantic and instance segmentation of road users (different vehicles and humans). From the instance labeling, we obtain the center points and bounding box ground truth of the objects.

**Evaluation metrics.** To evaluate the calibration of our method, we use the expected calibration error Naeini et al. [2015]. The ECE splits the confidence space into several bins and calculates the observed accuracy in each bin. The gaps between the confidence and the observed accuracy of the bins are summed and weighted by the number of samples in each bin.

## 4.3 Numerical results

**PPP intensity calibration.** In this section, we compare our intensity prediction of the PPP with the semantic segmentation prediction regarding the respective calibration of predicting empty spaces. The question we are considering here is whether a particular region  $A$  contains objects or whether it is drivable. Semantic segmentation is the pixel-wise classification of image content into predefined semantic classes. A DNN given an input image  $I_d$  and learned weights provides for pixel  $\pi \in P$  a probability distribution specifying the probability for each class  $\kappa \in \mathcal{C}$  denoted by  $p(\kappa|I_d)_\pi \in [0, 1]$ . The probability that a region is drivable is given by  $\mathbb{P}_S(A \text{ is drivable}) = \prod_{\pi \in \Pi(A)} p(\text{“road”}|I_d)_\pi$ , as the pixel predictions are assumed to be independent when conditioned on a fixed image  $I$ . We consider a region to be drivable if it contains no classes other than “road”. For the PPP method, the probability that the region is free is derived from the case  $n = 0$  in eq. (1) under the discretization (8)

$$\mathbb{P}_P(A \text{ is drivable}) = \exp\left(-\int_A \lambda(\xi) d\xi\right) \approx \exp\left(-\sum_{\pi \in \Pi(A)} \lambda(\pi)\varepsilon_x\varepsilon_y\right), \quad (13)$$

i.e., no object is predicted. We consider a region to be drivable if it contains no object center point.

To determine the calibration of the methods, we sample random boxes (test regions) of a fixed area  $s$  (height and width are also chosen randomly), whereby the number of boxes per image is fixed (here 50). For each box, we determine whether it is drivable and determine the respective probability, from which the ECE metric is then calculated. The results depending on the test box size are shown in Table 1. We observe that calibration for smaller boxes also achieves smaller ECE errors. Furthermore, we find that HRNet is more accurately calibrated than DeepLabv3+ for semantic segmentation. The reason for this could be the difference in model capacity and that HRNet does not use significant downsampling or pyramid architecture, instead relying on high-resolution representations through the whole process. These differences between the models vanish with our PPP method. It is quite evident that our PPP method is significantly better calibrated than the semantic segmentation prediction. A corresponding confidence calibration plot is shown in Figure 3 (left). The semantic segmentation prediction is consistently underconfident; if there is any uncertainty that the area is drivable, the confidence tends toward zero which is expected from the confidence factorization. In comparison, our method fluctuates close to the optimal calibration (gray diagonal in the plot).

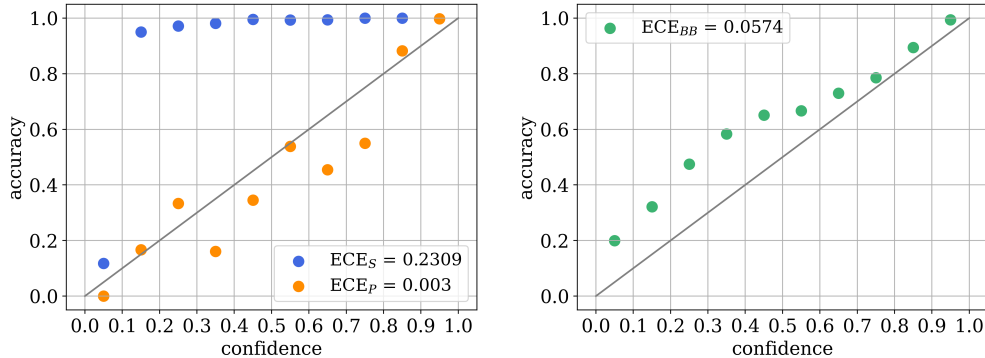


Figure 3: Confidence calibration plots for semantic segmentation (blue), PPP (orange) and CMPPP (green) with corresponding ECE values for the DeepLabv3+ based model and a  $s = 1,000$ .

Table 2: Calibration values for our object detector ( $ECE_{BB}$ ) for different box sizes  $s$ .

|            | 250    | 500    | 750    | 1,000  | 1,500  | 2,500  | 5,000  | 10,000 |
|------------|--------|--------|--------|--------|--------|--------|--------|--------|
| DeepLabv3+ | 0.0775 | 0.0698 | 0.0625 | 0.0574 | 0.0578 | 0.0567 | 0.0569 | 0.0683 |
| HRNet      | 0.0825 | 0.0750 | 0.0709 | 0.0641 | 0.0647 | 0.0631 | 0.0621 | 0.0750 |

**Bounding box detection.** Using our CMPPP model, instead of the center point of an object, we receive a bounding box prediction with the corresponding class and score value. The latter reflects the probability (12) that a region is drivable, whereby we use the Laplace distribution function as in eq. (12) due to training with the  $L^1$ -loss. An example of CMPPP confidence and the bounding box prediction is shown in Figure 1 (see appendix A.2 for further visualizations<sup>2</sup>). We observe the differences in intensity between the objects more clearly than with the PPP because box height and width contribute to the confidence level.

In this object detection application, we consider a test regions to be drivable if the test box and the ground truth bounding box do not overlap. In the same way as before, we sample 50 random test boxes of a fixed size  $s$  per image to evaluate the calibration. The results depending on  $s$  are given in Table 2, and a corresponding confidence calibration plot is shown in Figure 3 (right). We achieve smaller errors, i.e., improved calibrations, compared to semantic segmentation and slightly worse values compared to PPP predictions. While the PPP only predicts the center points of objects, CMPPP adds the prediction of the height and width of the bounding box, which is more challenging for confidence calibration. We observe again a similar calibration of the DeepLabv3+ and the HRNet. However, for both architectures we do not identify a clear trend between error and box size.

Object detection is usually evaluated using mean average precision (mAP), which assesses detection capability and accuracy. On the two classes, persons and vehicles, the DeepLabv3+ model achieves a mAP of 51.19% and HRNet 54.28%. In comparison, Faster R-CNN Ren et al. [2015], a well-known object detection network, on the Cityscapes images obtains a mAP value of 59.32%. Despite marginally lower performance, we are able to more reliably predict empty spaces than normal object detection methods.

## 5 Limitations

Our proposed two-stage training scheme prevents a true end-to-end training of the model and likely decreases object detection performance of the full model. Further, the architectural design illustrated in Figure 2 is likely not optimally efficient since the two encoder-decoder networks require more parameters (even if it is only an added shallow UNet) slowing down inference time. The architecture might benefit from sharing extracted features from the primary FCNN directly with the detection heads. In Figure 3, we saw still small amount of miscalibration of both models which we hypothesize is due to the fact that the model invested significant amounts of capacity to be well-calibrated on

<sup>2</sup>A public demonstration video can be found under <https://www.youtube.com/watch?v=1zS1ajNSN-E>.

$\mathbb{P}(N(A) = n|I)$  for any  $n$  appearing in the training data with no particular stress on exactly  $n = 0$ . Finally, road participants and obstacles occupy physical space while we only account for “free” point configurations in our model, not incorporating interaction potentials between events.

## 6 Conclusion

In this work, we have introduced a novel object detection architecture and learning objective guided by the question “With what probability is some particular region of the input image devoid of objects, i.e., drivable?”. Following a principled approach based on the theory of spatial point processes, we have derived an object detection model which may be trained by a notion of negative log-likelihood to model the object intensity function over the input image. Modeling the point configuration with shape and class distribution markings constitutes an object detection model capable of assigning a meaningful confidence to the event of a test region intersecting any predicted object in the image. We investigate two instances of our model on the Cityscapes dataset and show in numerical experiments that it is capable of solid object detection performance and is well-calibrated on emptiness. Compared to semantic segmentation, we obtain significantly better confidence calibration, and compared to common object detectors, we also obtain reliable information about object-free areas.

## Acknowledgments and Disclosure of Funding

Funding by the Federal Ministry for Economic Affairs and Energy (BMWE) through the Safe AI Engineering consortium grant no. 19A24000U is gratefully acknowledged.

## References

- Joao Cartucho, Samyakh Tukra, Yunpeng Li, Daniel S. Elson, and Stamatia Giannarou. Visionblender: a tool to efficiently generate computer vision datasets for robotic surgery. *Computer Methods in Biomechanics and Biomedical Engineering: Imaging & Visualization*, 9(4):331–338, 2021. doi: 10.1080/21681163.2020.1835546.
- Yu-Ching Chan, Yu-Chen Lin, and Peng-Cheng Chen. Lane mark and drivable area detection using a novel instance segmentation scheme. In *2019 IEEE/SICE International Symposium on System Integration (SII)*, pages 502–506, 2019. doi: 10.1109/SII.2019.8700359.
- Yicong Chang, Feng Xue, Fei Sheng, Wenteng Liang, and Anlong Ming. Fast road segmentation via uncertainty-aware symmetric network. In *2022 International Conference on Robotics and Automation (ICRA)*, page 11124–11130. IEEE Press, 2022. doi: 10.1109/ICRA46639.2022.9812452.
- Kai Chen, Jiaqi Wang, Jiangmiao Pang, Yuhang Cao, Yu Xiong, Xiaoxiao Li, Shuyang Sun, Wansen Feng, Ziwei Liu, Jiarui Xu, Zheng Zhang, Dazhi Cheng, Chenchen Zhu, Tianheng Cheng, Qijie Zhao, Buyu Li, Xin Lu, Rui Zhu, Yue Wu, Jifeng Dai, Jingdong Wang, Jianping Shi, Wanli Ouyang, Chen Change Loy, and Dahua Lin. MMDetection: Open mmlab detection toolbox and benchmark. *arXiv preprint arXiv:1906.07155*, 2019.
- Liang-Chieh Chen, Yukun Zhu, George Papandreou, Florian Schroff, and Hartwig Adam. Encoder-decoder with atrous separable convolution for semantic image segmentation. In Vittorio Ferrari, Martial Hebert, Cristian Sminchisescu, and Yair Weiss, editors, *European Conference on Computer Vision (ECCV)*, pages 833–851, Cham, 2018. Springer International Publishing. doi: 10.1007/978-3-030-01234-2\_49.
- Xing Chen, Yujiao Dong, Xinyong Li, Xunjia Zheng, Hui Liu, and Tengyuan Li. Drivable area recognition on unstructured roads for autonomous vehicles using an optimized bilateral neural network. In *Scientific Reports*, 2025. doi: 10.1038/s41598-025-94655-1.
- Marius Cordts, Mohamed Omran, Sebastian Ramos, Timo Rehfeld, Markus Enzweiler, Rodrigo Benenson, Uwe Franke, Stefan Roth, and Bernt Schiele. The cityscapes dataset for semantic urban scene understanding. In *2016 IEEE Conference on Computer Vision and Pattern Recognition (CVPR)*, pages 3213–3223, Los Alamitos, CA, USA, jun 2016. IEEE Computer Society. doi: 10.1109/CVPR.2016.350.

- Daryl J Daley and David Vere-Jones. *An introduction to the theory of point processes: volume I: elementary theory and methods*. Springer Science & Business Media, 2006.
- Rui Fan, Hengli Wang, Peide Cai, and Ming Liu. Sne-roadseg: Incorporating surface normal information into semantic segmentation for accurate freespace detection. In Andrea Vedaldi, Horst Bischof, Thomas Brox, and Jan-Michael Frahm, editors, *Computer Vision – ECCV 2020*, pages 340–356, Cham, 2020. Springer International Publishing. ISBN 978-3-030-58577-8.
- K. Ruwani M. Fernando and Chris P. Tsokos. Dynamically weighted balanced loss: Class imbalanced learning and confidence calibration of deep neural networks. *IEEE Transactions on Neural Networks and Learning Systems*, 33(7):2940–2951, 2022. doi: 10.1109/TNNLS.2020.3047335.
- Yarin Gal and Zoubin Ghahramani. Dropout as a bayesian approximation: Representing model uncertainty in deep learning. In *Proceedings of the 33rd International Conference on International Conference on Machine Learning - Volume 48, ICML’ 16*, pages 1050–1059. JMLR.org, 2016.
- Chuan Guo, Geoff Pleiss, Yu Sun, and Kilian Q. Weinberger. On calibration of modern neural networks. In *Proceedings of the 34th International Conference on Machine Learning - Volume 70, ICML’ 17*, page 1321–1330. JMLR.org, 2017.
- Juan Luis Hortelano, Jorge Villagr a, Jorge Godoy, and V ctor Jim nez. Recent developments on drivable area estimation: A survey and a functional analysis. *Sensors*, 23(17), 2023. ISSN 1424-8220. doi: 10.3390/s23177633.
- Mahek Jain, Guruprasad Kamat, Rochan Bachari, Vinayak A. Belludi, Dikshit Hegde, and Ujwala Patil. Affordrive: Detection of drivable area for autonomous vehicles. In Pradipta Maji, Tingwen Huang, Nikhil R. Pal, Santanu Chaudhury, and Rajat K. De, editors, *Pattern Recognition and Machine Intelligence*, pages 532–539, Cham, 2023. Springer Nature Switzerland. ISBN 978-3-031-45170-6.
- Byeongmoon Ji, Hyemin Jung, Jihyeun Yoon, Kyungyul Kim, and younghak Shin. Bin-wise Temperature Scaling (BTS): Improvement in Confidence Calibration Performance through Simple Scaling Techniques . In *2019 IEEE/CVF International Conference on Computer Vision Workshop (ICCVW)*, pages 4190–4196, Los Alamitos, CA, USA, October 2019. IEEE Computer Society. doi: 10.1109/ICCVW.2019.00515.
- J. Kang and J. Gwak. Ensemble of instance segmentation models for polyp segmentation in colonoscopy images. *IEEE Access*, 7:26440–26447, 2019. doi: 10.1109/ACCESS.2019.2900672.
- Meelis Kull, Telmo Silva Filho, and Peter Flach. Beta calibration: a well-founded and easily implemented improvement on logistic calibration for binary classifiers. In Aarti Singh and Jerry Zhu, editors, *Proceedings of the 20th International Conference on Artificial Intelligence and Statistics*, volume 54 of *Proceedings of Machine Learning Research*, pages 623–631. PMLR, 20–22 Apr 2017.
- Meelis Kull, Miquel Perello-Nieto, Markus K ngsepp, Telmo Silva Filho, Hao Song, and Peter Flach. Beyond temperature scaling: obtaining well-calibrated multiclass probabilities with dirichlet calibration. In *Proceedings of the 33rd International Conference on Neural Information Processing Systems*, Red Hook, NY, USA, 2019. Curran Associates Inc.
- Ananya Kumar, Percy S Liang, and Tengyu Ma. Verified uncertainty calibration. In H. Wallach, H. Larochelle, A. Beygelzimer, F. d’Alch -Buc, E. Fox, and R. Garnett, editors, *Advances in Neural Information Processing Systems*, volume 32. Curran Associates, Inc., 2019.
- Aviral Kumar, Sunita Sarawagi, and Ujjwal Jain. Trainable calibration measures for neural networks from kernel mean embeddings. In Jennifer Dy and Andreas Krause, editors, *Proceedings of the 35th International Conference on Machine Learning*, volume 80 of *Proceedings of Machine Learning Research*, pages 2805–2814. PMLR, 10–15 Jul 2018.
- Fabian K ppers, Anselm Haselhoff, Jan Kronenberger, and Jonas Schneider. *Confidence Calibration for Object Detection and Segmentation*, pages 225–250. Springer International Publishing, Cham, 2022. ISBN 978-3-031-01233-4. doi: 10.1007/978-3-031-01233-4\_8.

- Balaji Lakshminarayanan, Alexander Pritzel, and Charles Blundell. Simple and scalable predictive uncertainty estimation using deep ensembles. In *Proceedings of the 31st International Conference on Neural Information Processing Systems*, NIPS'17, pages 6405–6416, USA, 2017. Curran Associates Inc. ISBN 978-1-5108-6096-4.
- Dong-Gyu Lee. Fast drivable areas estimation with multi-task learning for real-time autonomous driving assistant. *Applied Sciences*, 11(22), 2021. ISSN 2076-3417. doi: 10.3390/app112210713.
- Tsung-Yi Lin, Piotr Dollar, Ross Girshick, Kaiming He, Bharath Hariharan, and Serge Belongie. Feature pyramid networks for object detection. In *Proceedings of the IEEE Conference on Computer Vision and Pattern Recognition (CVPR)*, July 2017.
- Yuchi Liu, Lei Wang, Yuli Zou, James Zou, and Liang Zheng. Optimizing calibration by gaining aware of prediction correctness, 2024.
- Tong Luo, Yanyan Chen, Tianyu Luan, Baixiang Cai, Long Chen, and Hai Wang. Ids-model: An efficient multitask model of road scene instance and drivable area segmentation for autonomous driving. *IEEE Transactions on Transportation Electrification*, 10(1):1454–1464, 2024. doi: 10.1109/TTE.2023.3293495.
- Yecheng Lyu, Lin Bai, and Xinming Huang. Road segmentation using cnn and distributed lstm. In *2019 IEEE International Symposium on Circuits and Systems (ISCAS)*, pages 1–5, 2019. doi: 10.1109/ISCAS.2019.8702174.
- Kira Maag and Tobias Riedlinger. Pixel-wise gradient uncertainty for convolutional neural networks applied to out-of-distribution segmentation. *International Joint Conference on Computer Vision, Imaging and Computer Graphics Theory and Applications (VISAPP)*, pages 112–122, 2024. doi: 10.5220/0012353300003660.
- Alireza Mehrtash, William M. Wells, Clare M. Tempny, Purang Abolmaesumi, and Tina Kapur. Confidence calibration and predictive uncertainty estimation for deep medical image segmentation. *IEEE Transactions on Medical Imaging*, 39:3868–3878, 2019.
- Jesper Møller, P. Bickel, Peter J. Diggle, S. Fienberg, K. Krickeberg, I. Olkin, N. Wermuth, and S. Zeger, editors. *Spatial Statistics and Computational Methods*, volume 173 of *Lecture Notes in Statistics*. Springer, New York, NY, 2003. ISBN 978-0-387-00136-4 978-0-387-21811-3. doi: 10.1007/978-0-387-21811-3.
- Jishnu Mukhoti, Viveka Kulharia, Amartya Sanyal, Stuart Golodetz, Philip H. S. Torr, and Puneet K. Dokania. Calibrating deep neural networks using focal loss. In *Proceedings of the 34th International Conference on Neural Information Processing Systems*, NIPS '20, Red Hook, NY, USA, 2020. Curran Associates Inc. ISBN 9781713829546.
- Mahdi Pakdaman Naeini, Gregory F. Cooper, and Milos Hauskrecht. Obtaining well calibrated probabilities using bayesian binning. In *Proceedings of the Twenty-Ninth AAAI Conference on Artificial Intelligence*, AAAI'15, page 2901–2907. AAAI Press, 2015. ISBN 0262511290.
- Gabriel Pereyra, George Tucker, Jan Chorowski, Łukasz Kaiser, and Geoffrey Hinton. Regularizing neural networks by penalizing confident output distributions, 2017.
- John C. Platt. Probabilistic outputs for support vector machines and comparisons to regularized likelihood methods. In *Advances in Large Margin Classifiers*, pages 61–74. MIT Press, 1999.
- Yeqiang Qian, John M. Dolan, and Ming Yang. Dlt-net: Joint detection of drivable areas, lane lines, and traffic objects. *IEEE Transactions on Intelligent Transportation Systems*, 21(11):4670–4679, 2020. doi: 10.1109/TITS.2019.2943777.
- Donghao Qiao and Farhana Zulkernine. Drivable area detection using deep learning models for autonomous driving. In *2021 IEEE International Conference on Big Data (Big Data)*, pages 5233–5238, 2021. doi: 10.1109/BigData52589.2021.9671392.
- Joseph Redmon, Santosh Divvala, Ross Girshick, and Ali Farhadi. You Only Look Once: Unified, Real-Time Object Detection . In *2016 IEEE Conference on Computer Vision and Pattern Recognition (CVPR)*, pages 779–788, Los Alamitos, CA, USA, June 2016. IEEE Computer Society. doi: 10.1109/CVPR.2016.91.

- Shaoqing Ren, Kaiming He, Ross Girshick, and Jian Sun. Faster r-cnn: Towards real-time object detection with region proposal networks. In C. Cortes, N. Lawrence, D. Lee, M. Sugiyama, and R. Garnett, editors, *Advances in Neural Information Processing Systems*, volume 28. Curran Associates, Inc., 2015.
- Olaf Ronneberger, Philipp Fischer, and Thomas Brox. U-Net: Convolutional Networks for Biomedical Image Segmentation. In Nassir Navab, Joachim Hornegger, William M. Wells, and Alejandro F. Frangi, editors, *Medical Image Computing and Computer-Assisted Intervention – MICCAI 2015*, Lecture Notes in Computer Science, pages 234–241, Cham, 2015. Springer International Publishing. ISBN 978-3-319-24574-4. doi: 10.1007/978-3-319-24574-4\_28.
- Michael Sherman. *Spatial statistics and spatio-temporal data: covariance functions and directional properties*. John Wiley & Sons, 2011.
- Jee-Young Sun, Seung-Wook Kim, Sang-Won Lee, Ye-Won Kim, and Sung-Jea Ko. Reverse and boundary attention network for road segmentation. In *2019 IEEE/CVF International Conference on Computer Vision Workshop (ICCVW)*, pages 876–885, 2019. doi: 10.1109/ICCVW.2019.00116.
- Huinian Wang, Jingyao Wang, Baoping Xiao, Yizhou Jiao, and Jinghua Guo. Drivable area and lane line detection model based on semantic segmentation. In *2024 IEEE 3rd International Conference on Computing and Machine Intelligence (ICMI)*, pages 1–7, 2024. doi: 10.1109/ICMI60790.2024.10585878.
- Jingdong Wang, Ke Sun, Tianheng Cheng, Borui Jiang, Chaorui Deng, Yang Zhao, Dong Liu, Yadong Mu, Mingkui Tan, Xinggang Wang, Wenyu Liu, and Bin Xiao. Deep high-resolution representation learning for visual recognition. *IEEE Transactions on Pattern Analysis and Machine Intelligence*, 2021.
- Mitchell Wortsman, Gabriel Ilharco, Samir Ya Gadre, Rebecca Roelofs, Raphael Gontijo-Lopes, Ari S Morcos, Hongseok Namkoong, Ali Farhadi, Yair Carmon, Simon Kornblith, and Ludwig Schmidt. Model soups: averaging weights of multiple fine-tuned models improves accuracy without increasing inference time. In Kamalika Chaudhuri, Stefanie Jegelka, Le Song, Csaba Szepesvari, Gang Niu, and Sivan Sabato, editors, *Proceedings of the 39th International Conference on Machine Learning*, volume 162 of *Proceedings of Machine Learning Research*, pages 23965–23998. PMLR, 2022.
- J. Xu, Z. Xiong, and S. P. Bhattacharyya. Pidnet: A real-time semantic segmentation network inspired by pid controllers. In *2023 IEEE/CVF Conference on Computer Vision and Pattern Recognition (CVPR)*, pages 19529–19539, Los Alamitos, CA, USA, 2023. IEEE Computer Society. doi: 10.1109/CVPR52729.2023.01871.
- B. Yan, Y. Jiang, J. Wu, D. Wang, P. Luo, Z. Yuan, and H. Lu. Universal instance perception as object discovery and retrieval. In *2023 IEEE/CVF Conference on Computer Vision and Pattern Recognition (CVPR)*, pages 15325–15336, Los Alamitos, CA, USA, 2023. IEEE Computer Society. doi: 10.1109/CVPR52729.2023.01471.
- Yue Yu, Yanhui Lu, Pengyu Wang, Yifei Han, Tao Xu, and Jianhua Li. Drivable area detection in unstructured environments based on lightweight convolutional neural network for autonomous driving car. *Applied Sciences*, 13(17), 2023. ISSN 2076-3417. doi: 10.3390/app13179801.
- Bianca Zadrozny and Charles Elkan. Obtaining calibrated probability estimates from decision trees and naive bayesian classifiers. In *Proceedings of the Eighteenth International Conference on Machine Learning, ICML '01*, page 609–616, San Francisco, CA, USA, 2001. Morgan Kaufmann Publishers Inc. ISBN 1558607781.
- Bianca Zadrozny and Charles Elkan. Transforming classifier scores into accurate multiclass probability estimates. In *Proceedings of the Eighth ACM SIGKDD International Conference on Knowledge Discovery and Data Mining, KDD '02*, page 694–699, New York, NY, USA, 2002. Association for Computing Machinery. ISBN 158113567X. doi: 10.1145/775047.775151.
- Z. Zong, G. Song, and Y. Liu. Detrs with collaborative hybrid assignments training. In *2023 IEEE/CVF International Conference on Computer Vision (ICCV)*, pages 6725–6735, Los Alamitos, CA, USA, 2023. IEEE Computer Society. doi: 10.1109/ICCV51070.2023.00621.

## A Appendix / supplemental material

### A.1 Computation of the Radon Nikodym derivative and negative log-likelihood

In this appendix we provide the computations which lead to equations (6) and (7) for the convenience of the reader. For the ease of notation, we perform this computation for the non-marked point process and omit conditioning on the image  $I$ .

Let thus  $\mu$  be the standard PPP on  $\Gamma$  with intensity 1 and let  $\frac{d\mu_\theta}{d\mu}(x)$  be given by eq. (6). We have to show that

$$d\mu_\theta(x) = \frac{d\mu_\theta}{d\mu}(x)d\mu(x)$$

fulfills the statistics given by eq. (1). Let thus  $\lambda_\theta(\xi)$  be the intensity function and  $A \subseteq [0, 1]^2$ , then the random variable counting the points in  $A$  can be represented as  $N(A)(\xi) = \sum_{j=1}^n \mathbb{1}_A(\xi_j)$  for  $x = (x_1, \dots, \xi_n) \in \Gamma$ . Under the standard PPP  $\mu$ , we have  $n \sim \text{Pois}(1)$ , and  $\xi_j \sim d\xi|_{[0,1]^2}$ .

To prove eq. (1), by Bochner's theorem it is enough to check for the identity of the Fourier transform of the distribution. We obtain for  $\tau \in \mathbb{R}$

$$\begin{aligned} \mathbb{E}_\mu \left[ e^{i\tau N(A)} \frac{d\mu_\theta}{d\mu} \right] &= \sum_{n=0}^{\infty} \frac{e^{-1}}{n!} \mathbb{E}_\mu \left[ e^{i\tau N(A)} \frac{d\mu_\theta}{d\mu} \middle| N([0, 1]^2) = n \right] \\ &= \sum_{n=0}^{\infty} \frac{e^{-1}}{n!} e^{-\int_{[0,1]^2} (\lambda_\theta(\xi) - 1) d\xi} \\ &\quad \times \int_{[0,1]^2} \cdots \int_{[0,1]^2} \left( \prod_{l=1}^n \lambda_\theta(\xi_l) \right) e^{i\tau \sum_{l=1}^n \mathbb{1}_A(\xi_l)} d\xi_1 \cdots d\xi_n \\ &= e^{-\int_{[0,1]^2} \lambda_\theta(\xi) d\xi} \sum_{n=0}^{\infty} \frac{1}{n!} \left( \int_{[0,1]^2} \lambda_\theta(\xi) e^{i\tau \mathbb{1}_A(\xi)} d\xi \right)^n \\ &= \exp \left( \int_{[0,1]^2} (e^{i\tau \mathbb{1}_A(\xi)} - 1) \lambda_\theta(\xi) d\xi \right) = \exp \left( \int_A \lambda_\theta(\xi) d\xi (e^{i\tau} - 1) \right), \end{aligned}$$

which gives the Fourier transform of the Poisson distribution with intensity parameter  $\int_A \lambda_\theta(\xi) d\xi$ , exactly as the Poisson distribution in eq. (1).

Let us now consider the computation leading to the expression of the negative log likelihood in eq. (7). we start with the relative density given in density equation (6) and compute the negative logarithm. This amounts to

$$\int_{[0,1]^2} \lambda_\theta(\xi) d\xi - 1 + \sum_{l=1}^n \log(\lambda_\theta(\xi_l)),$$

replacing  $\lambda_\theta(\xi_l)$  with  $e^{L_\theta(\xi_l|I_d)}$  and canceling the exponential function with the log. This gives, up to an irrelevant additive term  $-1$  the first two terms in eq. (7).

Like in the product in eq. (6), for a marked particle configuration  $x = ((\xi_1, m_1), \dots, (\xi_n, m_n))$ , the product in the density eq. (6) for the marked PPP now by eq. (3) includes additional factors  $p(m_l|\xi_l, I_d)$ . Note that the pre-factor  $e^{\int_{[0,1]^2} (\lambda_\theta(\xi) - 1) d\xi}$  remains unchanged when replacing  $\lambda$  by  $\Lambda$  as  $\int_M p(m_l|\xi_l, I_d) dm = 1$ . To evaluate the negative log likelihood of the additional product factors, we have to insert the second equation in eq. (4) to evaluate  $p(m_l|\xi_l, I_d)$ . This provides

$$\log \left( \prod_{l=1}^n p(m_l|\xi_l, I) \right) = \sum_{l=1}^n \log \left( \frac{1}{2\sigma} e^{-\frac{1}{\sigma} \left\| \begin{pmatrix} w_l \\ h_l \end{pmatrix} - B_{\theta_B}(\xi_l, I_d) \right\|_1 [\text{softmax}(C_{\theta_C}(\xi_l, w_l, h_l, I_d))]_{\kappa_l}} \right)$$

and following the computation rules for the logarithm, we arrive at eq. (7). Note that here we also use that  $\text{softmax}(C)_\kappa = \frac{e^{C_\kappa}}{\sum_{\kappa' \in \mathcal{C}} e^{C_{\kappa'}}}$  and thus  $\log(\text{softmax}(C)_\kappa) = C_\kappa - \log(\sum_{\kappa' \in \mathcal{C}} e^{C_{\kappa'}})$ .



Figure 4: *Left*: Semantic segmentation prediction. *Center left*: Poisson point process intensity. *Center right*: Conditional marked Poisson point process intensity. *Right*: Bounding box prediction.

Table 3: Calibration values for our object detector trained with  $L^2$ -loss for different box sizes  $s$ .

|            | 250    | 500    | 750    | 1,000  | 1,500  | 2,500  | 5,000  | 10,000 |
|------------|--------|--------|--------|--------|--------|--------|--------|--------|
| DeepLabv3+ | 0.0795 | 0.0724 | 0.0642 | 0.0587 | 0.0578 | 0.0550 | 0.0541 | 0.0668 |

## A.2 More numerical results

**Visual Results.** In Figure 4, we show more qualitative examples, i.e., PPP and CMPPP intensity heatmaps as well as the corresponding bounding box prediction.

**Gaussian Residuals.** In Section 3, we discussed a CMPPP model with Laplace-distributed residuals which leads to training based on the  $L^1$  regression loss. While this is a widely spread approach to bounding box regression, we may analogously model the residuals as normal distributions by adjusting  $p_{\theta_B, \theta_C, \sigma^2}$  in eq. (4). In eq. (12), we then require the cumulative distribution function of the normal distribution with the same mean parameters and variance  $\sigma^2$  determined analogously to the Laplace distribution as the mean squared error.

Resulting calibration errors are displayed in table 3. The calibration values are very similar to those in Table 2 (main paper). We see small deviations, with training using the  $L^1$ -loss yielding better values for smaller sampled boxes and slightly worse values for larger ones.